

# Flexible and Conformable Carbon Nanotube Twin Transistors for Real-Time Glucose Biosensing

Hanxiang Wu, Yu Song, Hexing Yin, Yuan Zhu, Ao Zhang, Zhixin Xie, Canran Wang, Meng Gao, Wei Gao, and Qibing Pei\*



Cite This: *ACS Appl. Nano Mater.* 2025, 8, 9924–9936



Read Online

ACCESS |

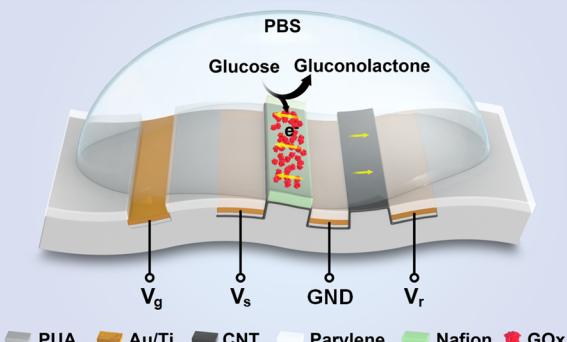
Metrics & More

Article Recommendations

Supporting Information

**ABSTRACT:** Semiconductive single-walled carbon nanotube (SWNT)-based transistors have long and extensively been explored for sensing applications, biosensors in particular, but reproducible reliable results remain elusive. The random distribution of the nanotube network, as well as the variation of the network due to deformation or surrounding fluidic dynamics, leads to fluctuation of the channel current, which is difficult to control. The signal-to-noise ratio is thus low, and calibration is required. To mitigate this challenge, SWNT-based twin transistors are introduced, where one acts as a sensor and the other as a reference. The twin transistors share gate and source electrodes, and all of the source/drain electrodes are sealed by a parylene layer to minimize electrolytic leakage. A common-source amplifier circuit generates voltage signal readouts from the sensor and reference transistors, and the differential outputs reduce the noise level by 59%. Arrays of twin transistors were fabricated in a hybrid process involving photolithography, solution-based deposition of the SWNTs, and transfer to a polyurethane substrate. To demonstrate glucose biosensing, glucose oxidase was immobilized on the SWNTs in the sensor channels. A semipermeable Nafion layer was applied to embed the SWNT network. This resulted in a sensor that can deliver real-time detection of glucose in human serum and a 100% increase in normalized responses per decade of glucose concentrations between 100  $\mu\text{M}$  and 100 mM. The response is proportional to the cubic root of glucose concentration, indicating that the redox electrons conducted by the nanotubes in the channel length direction contribute to the sensor response. A portable glucose-sensing system with flexible twin transistors is also demonstrated without the need for device-specific calibrations.

**KEYWORDS:** carbon nanotube transistors, glucose biosensing, microfabrication, noise-cancellation, conformal adhesion



## INTRODUCTION

Nanomaterial-based flexible transistors<sup>1–3</sup> show great potential in providing specific biomarker sensing in electrolytes, such as with human body fluids,<sup>4–7</sup> because flexible devices are more suitable for in vivo or in situ measurement as compared to rigid electronic devices. In addition, the nature of signal amplification in transistors plus the high surface-to-volume ratio of semiconducting nanomaterials, e.g., carbon nanotubes (CNTs), make it possible to achieve an unprecedented high sensitivity.<sup>8–13</sup> The current of CNT-based transistors can be altered by reactions between targets and immobilized receptors on transistor channels, which realizes multiple biomarker sensing in body fluids,<sup>14–20</sup> especially glucose.<sup>21–27</sup> And the immobilization of receptors can be achieved by using different methods such as polymer covering<sup>28–30</sup> and molecular linking.<sup>31–34</sup>

However, there are signal accuracy issues caused by the high leakage current<sup>35,36</sup> and fluctuations<sup>37–39</sup> in the electrolyte environment. An external gate electrode with movement relative to the channel area causes changes to the signal readout.<sup>40,41</sup> Baseline calibrations are necessitated with bulky semiconductor

analyzers, and their responses cannot be in real-time due to the complex data processing involved.<sup>42–44</sup> All of these issues illustrate the need for a practical, highly stable transistor for biosensing with innovative device structures, as well as delicate circuitries through electrical engineering designs.<sup>45–48</sup> Differential sensor architecture has been applied for increased signal stability in transistors for biosensing,<sup>49–55</sup> but rarely reported for CNT transistors.<sup>50</sup> Meanwhile, amplifier circuits for biosignal processing purposes based on flexible CNT transistors have been proposed,<sup>56–60</sup> which implies the feasibility of using such a strategy in direct biosensing with functionalization. The sensing technology of some biomarkers, e.g., glucose, is rather mature and commercially available. However, a general strategy for

Received: February 26, 2025

Revised: April 29, 2025

Accepted: May 2, 2025

Published: May 7, 2025



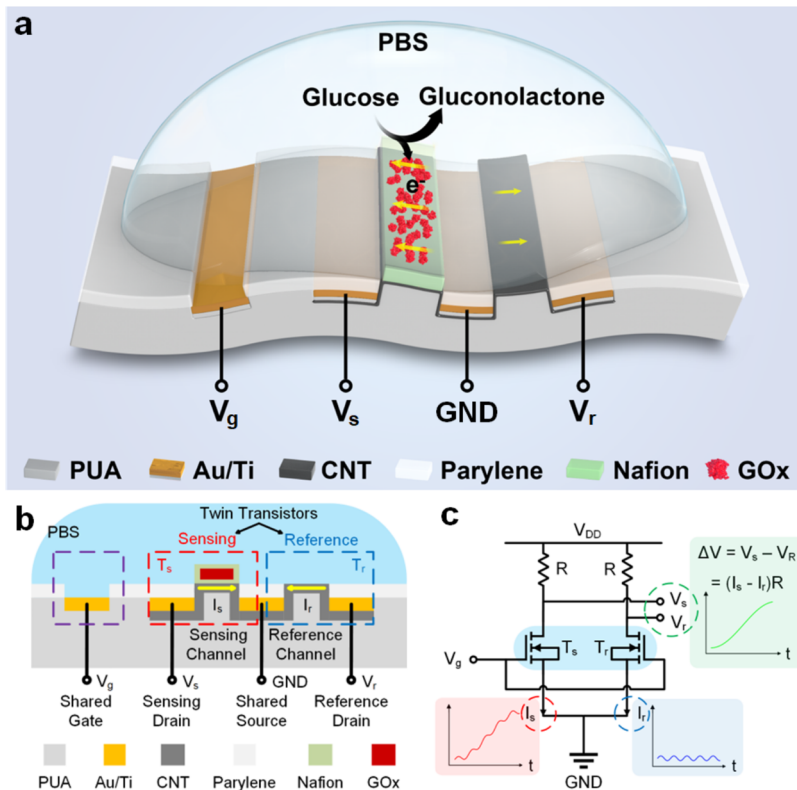


**Figure 1.** Illustration detailing a pair of SWNT twin transistors. (a) Schematic of the twin transistors' architecture and the enhanced current in the sensor channel when glucose is present. (Yellow arrows represent electron movement.) (b) Side view, where yellow arrows represent the current direction. (c) Circuit diagram of a differential common-source amplifier circuit. The twin transistors are shown in the blue shaded area.

accurate and stable functionalized transistor-based biomarker sensing is still of interest.

This paper details how we developed flexible and conformable carbon nanotube transistors that feature novel fabrication methods, device structures, and measuring circuits. We used a compatible method that combined microfabrication and solution-based processing with which the single-walled carbon nanotube (SWNT)-transistors were embedded into a polymer matrix. Photolithography was used for transistor layout, which enabled the process to produce high yields and resolutions. Moreover, the solution-based SWNT drop-casting method and polymer transferring process we used guarantee high performance for the transistors as biosensors. The channels and integrated gate areas were then exposed to electrolytes for biosensing, while the source and drain electrodes were encapsulated in thin parylene layers to minimize current leakage. An integrated gate electrode was used to replace the external gate electrode as this would reduce signal fluctuations and system complexity. We also employed a simple common-source amplifier that gives a direct voltage signal readout to achieve real-time sensing instead of processing transfer curves to introduce calibrated responses and thus cause a time delay. As for the signal fluctuations that are caused by the electrolyte environment, we created an integrated twin-transistor pair that acted as differential outputs, with one functionalized for sensing while the other acted as a reference to cancel out any noise. As the noise will generally cause the same level of fluctuation in the current of both transistors in the twin pair, it can be canceled by simply deducting one from the other. The measurement of the differential voltage enhances the sampling rates while simplifying the measuring circuit. We immobilized glucose oxidase

(GOx) with the use of a Nafion layer on the channel area of the sensing transistor to provide glucose sensing. The platform that we propose with carbon nanotube transistors will address current difficulties by delivering real-time and highly stable biosensing results.

**Device Structure and Circuit Design.** The device structure and its working principles are illustrated in Figure 1. An elastic polyurethane acrylate (PUA) thin film serves as the supporting substrate, and the gate electrode is coplanar with the channel area and source/drain electrodes on the substrate, as shown in Figure 1a. This architecture takes advantage of phosphate-buffered saline (PBS) or body fluid being employed as the gate electrolytic dielectric, and the source and drain electrodes are encapsulated with a parylene layer to prevent electrolytic current leakage. Two drain electrodes are located symmetrically from the shared source electrode, forming “twin transistors”, with one functioning as a sensor and the other one as a reference. The two channels use an identical SWNT network, which is deposited in the same process, except that in the sensing channel, the nanotubes are functionalized with glucose oxidase (GOx). The sensing channel area is over-coated with a layer of Nafion to immobilize the GOx beneath it. The Nafion layer also acts as a barrier that limits the diffusion of contaminating species into the channel, and the reference transistor has its SWNT channel directly exposed to the electrolytes. The side view in Figure 1b further illustrates the architecture of the twin transistors.

The equivalent circuit, i.e., the differential common-source amplifier that incorporates the twin transistors, is shown in Figure 1c. The blue shaded area in Figure 1c corresponds to the schematic of the twin transistors in Figure 1a,1b, and we adopted

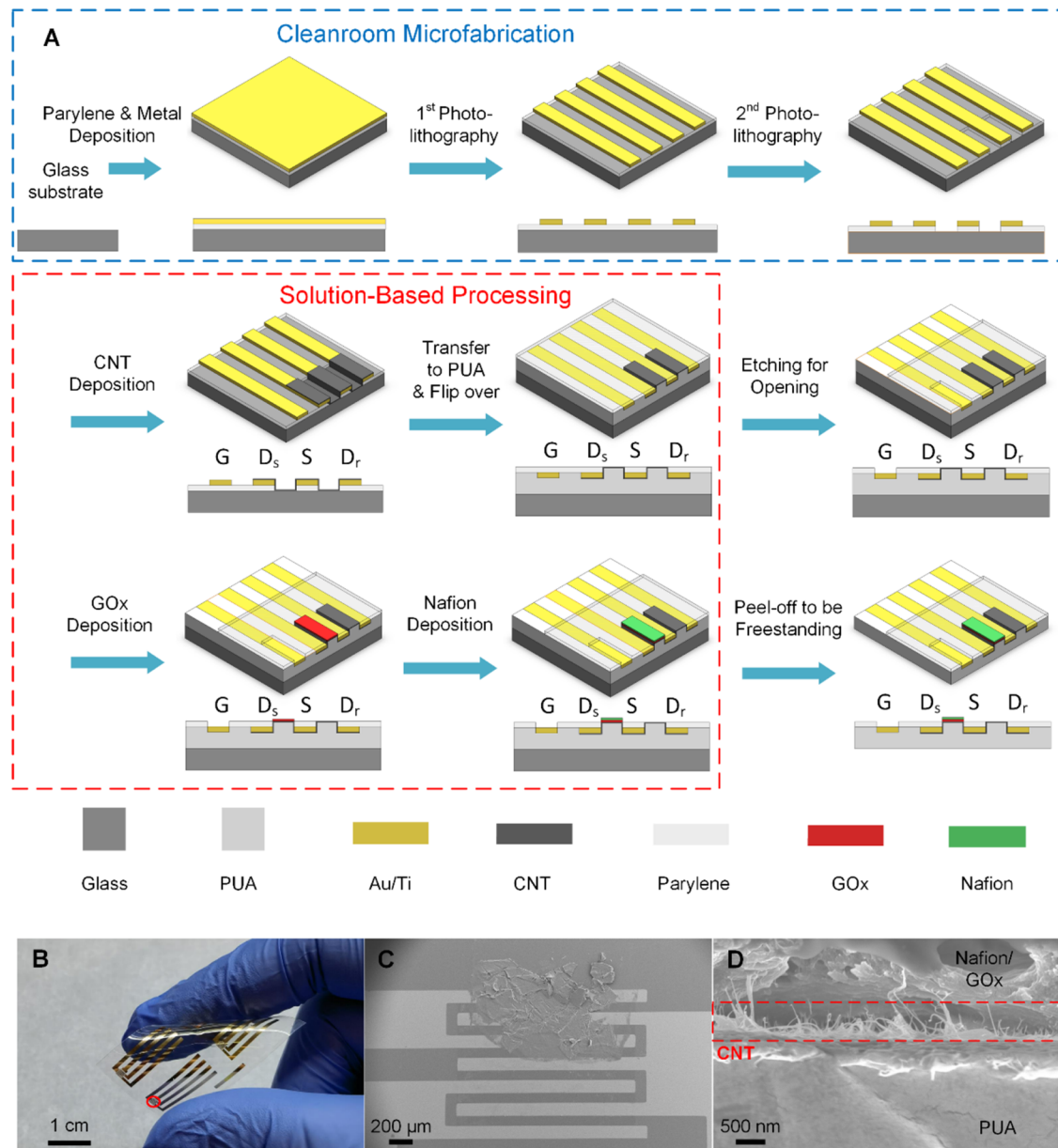


**Figure 2.** Schematic of the fabrication process and characterization of the fabrication result of the twin transistors. (A) Schematic of the fabrication process for a twin transistor glucose sensor. Both top and side views of the structures after each of the major steps are shown. (B) Optical photograph of a  $2 \times 2$  array of the twin transistors on a PUA substrate. (C) Scanning electron microscope (SEM) image of the channel area, with the upper half of the channel covered by Nafion. (D) Cross-sectional SEM image of the sensor channel revealing the SWNT, Nafion/GOx, and PUA.

a common-source amplifier as the basic component of the circuit. Composed of a transistor and a resistor, it is able to linearly amplify the current signal through the transistor into voltage signals across the resistor. The relationship between output voltage  $V$  and input current  $I$  for sensing and reference transistor is

$$V_s = V_{DD} - RI_s \quad (1)$$

$$V_r = V_{DD} - RI_r \quad (2)$$

where  $R$  is the resistance value for the externally connected resistors. The resistance  $R$  is chosen to be the largest possible value for the transistor to work in the saturation region when the drain current is at its maximum in response to glucose. In this way, the current signal is amplified to the largest extent, and the value  $R$  is chosen to be  $200\text{ k}\Omega$ . The amplification is essential for

measuring delicate signals. Different from the current signal, which requires bulky equipment to measure it, the voltage signal is friendlier, with simpler readout designs even by a single-chip board. In addition, continuous measuring of the voltage outputs will allow real-time readouts instead of sweeping discrete transfer curves, which have low sampling rates that require post-data processing like fitting to generate a delayed result.

Two symmetrical common-source amplifier circuits are used to form a differential circuit. A differential input/output design is adopted to allow for biosensing signals to be acquired with high accuracy and low complexity. As the transistors on the two branches will receive the same level of noise, this noise can be canceled out by simply subtracting the voltage values of each transistor's output without a scale factor and transmitting only the target-induced signal to the back-end processing unit. A

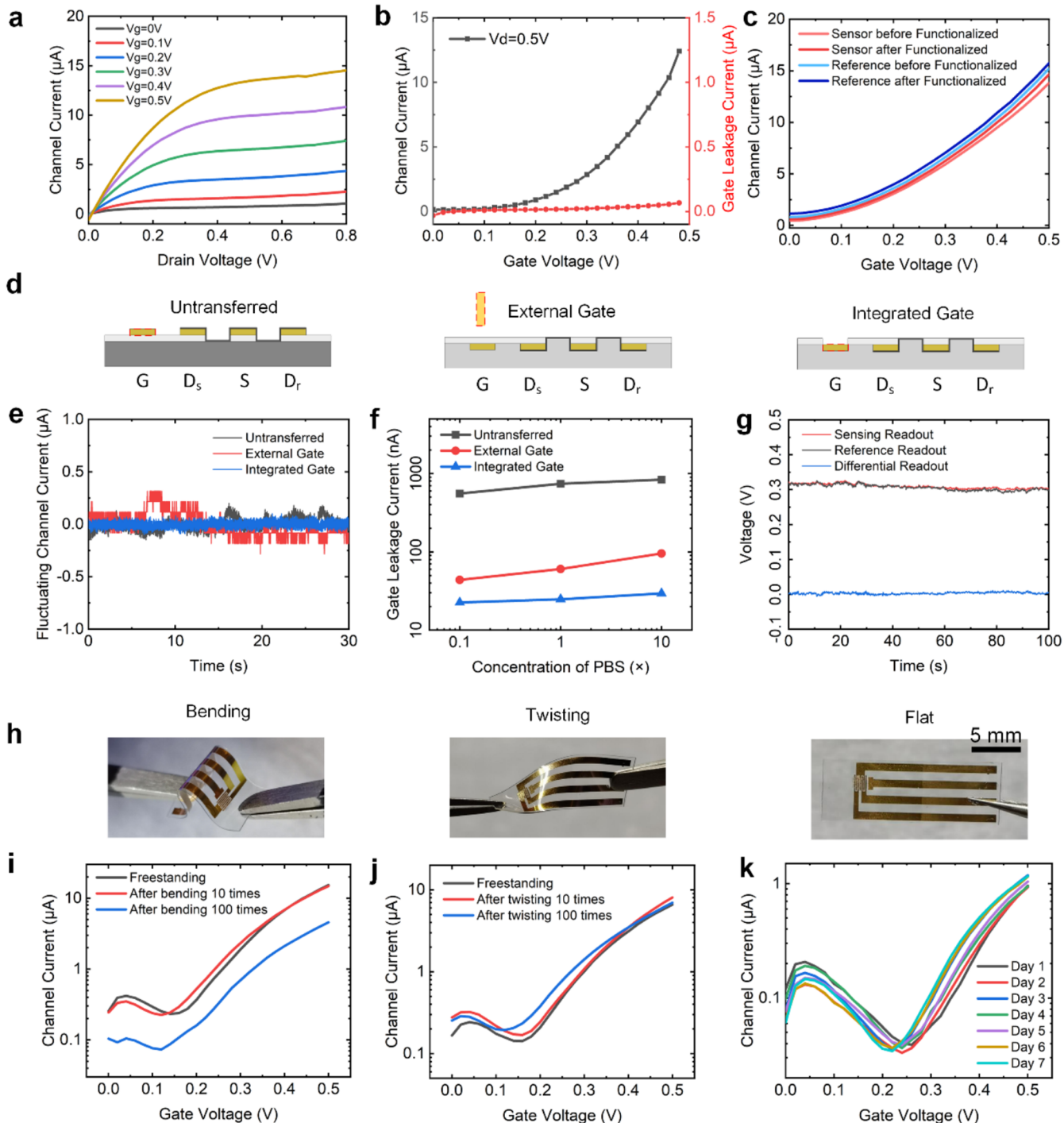


**Figure 3.** Electrical characterization of the transistors. (a) Output characteristics of a unit transistor. (b) Transfer characteristics of a unit transistor. (c) Comparison of the transfer curves before and after functionalization for the sensing and reference transistors. (d) Diagram of three device structures (i) without parylene encapsulation (untransferred), (ii) with an external gate electrode, and (iii) with an integrated gate electrode (standard). Please refer to Figure 2A for legends. (e) Measured baseline channel currents of the transistors (i), (ii), and (iii) by their parylene encapsulating layer and integrated gate. (f) Measured gate leakage current. (g) Voltage output of a twin transistor and the differential output. (h) Pictures showing the transistors in bent, twisted, and flat conditions. (i) Comparison of the transfer curves when freestanding and after being bent 10 times and 100 times, respectively. (j) Comparison of the transfer curves when freestanding and after being twisted 10 times and 100 times, respectively. (k) The transfer curves from day 1 to day 7 of the durability test.

differential circuit is especially suitable for the scenario here, as signal fluctuations from the electrolyte environment, e.g., ion movement fluctuations, will cause identical changes in the currents of both the twin transistors despite their functionalization status. Because the errors from the electrolyte environment

are canceled out, the differential signals will only reflect the target-induced differences between the sensing transistor and the reference transistor. As a result, this design can guarantee stable and accurate sensing results.

The design of the circuit thus plays a very important role in ensuring that real-time stable biosensing is achieved. The relationship between the real-time voltage readout  $\Delta V$  and currents on the two branches  $I_s$  and  $I_r$  is

$$\Delta V = V_s - V_r = (I_s - I_r)R \quad (3)$$

where  $R$  is the resistance of the resistor in the common-source amplifier circuit. The qualitative illustration in Figure 1c demonstrates the trends for  $I_s$ ,  $I_r$ , and  $\Delta V$ . After the  $I_s$  waveform subtracts the noise, which is represented by  $I_r$ , it will then reflect the accurate sensing result, which can be further amplified by a ratio of  $R$  to become  $\Delta V$ . The transistor current is mainly determined by the gate voltage, while it is slightly affected by the drain voltage. Changes in the electrolyte environment induced by the sensing target affect the transistor current, which is then used as the sensing parameter. A more detailed explanation of the circuit design can be found in Figure S1 and the Supporting Information Section 1 (page S-1).

**Fabrication of the Flexible and Conformable Carbon Nanotube Transistors.** Fabrication of the flexible and conformable carbon nanotube transistors was achieved by combining cleanroom-based microfabrication and solution-based processing, as illustrated by the flowcharts in Figure 2A. The first row in Figure 2A shows the cleanroom-based process, which includes the chemical vapor deposition of parylene and the vacuum evaporation of the metal layers, i.e., Au and Ti, respectively. Two photolithography processes were conducted sequentially to define the interdigitated electrodes and the channel areas, and then oxygen plasma etching was used to etch away the parylene in the channel areas to allow the SWNTs to be exposed to the electrolytes later.

In the second row of Figure 2A, the solution-based processing that was used for SWNT deposition and transferring is illustrated. A laser-cut polydimethylsiloxane (PDMS) contact mask was adopted and aligned to define the channel area for the SWNT deposition and to concentrate the dispersion in the vertical direction so that more of the SWNTs could be preserved in the channel area after the rinsing and drying. Drop-casting of SWNT dispersion was then performed on each of the channel regions. With a hydrophilic target surface induced by oxygen plasma treatment, carbon nanotubes could be distributed uniformly across the channel area once the solvent had vaporized; the PDMS mask would also protect the rest of the parylene from being etched by the oxygen plasma. Polyurethane acrylate was used as the polymer matrix for the transferring process because of its photocurable features and low Young's modulus. We were able to embed and transfer the SWNT network to the PUA substrate while ensuring that they bound with the parylene surface with the aid of 3-(trimethoxysilyl) propyl methacrylate (TMSPMA). All of these fabrication steps were deliberately designed so that they were able to deliver high yields as well as enable the transistors to perform as designed. After the parylene side was peeled off from the inkjet mold, and the contact openings were made using the oxygen plasma according to the areas defined by a second PDMS contact mask, the flexible twin transistors were then ready to be functionalized.

We adopted an agent-specific functionalization of the SWNT channel by immobilizing an enzyme, i.e., glucose oxidase (GOx), which had the ability to alter the electrical output of the transistor in response to glucose. The channel without receptor functionalization would serve as the reference. As exhibited in the third row of Figure 2A, a third PDMS contact mask was used to define the area to be functionalized, which would be above the

channel of the sensing transistor. A GOx solution was drop-cast onto this area and then dried. Nafion is a negatively charged soluble polymer that is also able to function as a molecular transfer membrane. After the Nafion was deposited in the channel area and covered the receptors beneath it, it was able to immobilize them while still allowing small molecules and ions to pass through it to complete the reaction. The device was ready for testing once test leads were connected to the electrodes. For more information regarding the fabrication process, please refer to the Materials section and Figure S2.

Figure S3a,b shows the exact geometry of the electrodes and channel patterns. Figure S3c displays a picture from an optical microscope that shows the pattern of an integrated device composed of one gate, one source, and two drain electrodes, respectively. The channel length of one finger is 100  $\mu\text{m}$ , its width is 1500  $\mu\text{m}$ , and each of the transistors consists of four fingers. Figure 2B is a photograph of one sheet of the fabricated devices that demonstrates their flexibility. Figure S3d displays a freestanding flexible sheet on a tweezer. The red circle in Figure 2B corresponds to the area shown in Figure 2C. Figure 2C is an SEM top view of the channel, which shows the sensing transistor covered by Nafion, while the reference transistor remains exposed. Figure 2D is an SEM image of the cross-section of the channel area that represents the SWNT embedded inside the polymer matrix and the GOx immobilized onto the channel area by Nafion. Figure S3e,f displays SEM images of the cross sections using smaller magnifications.

**Electrical Performance of the Twin Transistors.** The electrical performances of the transistors are characterized in Figure 3. The output and transfer curves are shown in Figure 3a and 3b, respectively. These curves indicate that the electrical properties of our transistor are comparable to that of a standard field-effect transistor (FET), even though the transistor is working in an electrolyte environment of 1× phosphate-buffered saline (PBS) with high ion strength, which would usually cause a degradation in the performance of a transistor. The expressions for the current of a typical field-effect transistor are

$$I = \alpha \left[ (V_g - V_{\text{th}})V_d - \frac{1}{2}V_d^2 \right] (1 + \lambda V_d) (V_d < V_g - V_{\text{th}}) \quad (4)$$

$$I = \alpha(V_g - V_{\text{th}})^2 (1 + \lambda V_d) (V_d \geq V_g - V_{\text{th}}) \quad (5)$$

where  $\alpha$  is a constant determined by the transistor's parameters,  $V_g$  is the gate voltage,  $V_{\text{th}}$  is the threshold voltage,  $V_d$  is the drain voltage, and  $\lambda$  is the scale factor for the unideal factor. Figure S4a demonstrates the case for these equations when  $\lambda = 0$ , and we can see that the curves in Figure 3a correspond well with eqs 4 and 5 when  $\lambda > 0$ . The n-type characteristics originated from the "inverted" position between the S/D electrodes and the semiconducting channel with respect to the gate of this device compared to most SWNT transistors with a gate-semiconductor-electrode structure from top to bottom. Figure S4b shows the transfer curve with negative  $V_g$  values in the logarithm scale, and the threshold voltage and subthreshold swing can be thus determined as  $-0.075$  V and 203 mV/dec, respectively. It is worth noticing that the liquid-gate transistor presented in this work mostly follows the classical transistor operation law, and we attribute this similarity to the fact that parylene insulation and CNT network embedding in polyurethane are adopted in the device structure so that minimal leakage current is conducted through the electrolyte. And we are able to base the differential measurement on the basis of the classical

transistor equations as long as the saturation region is mostly flat. A number of literature studies reporting liquid-date transistors also follow the classical transistor operation law.<sup>15,22,56</sup>

The current was around several  $\mu$ As when the condition of  $V_g = V_d = 0.5$  V, and current density reached 1  $\mu$ A/mm along the width direction. On the other hand, the drain current was about 1000 times that of the leakage current, which was in the order of 10 nA. A low leakage current guarantees a high signal-to-noise ratio (SNR) and, thus, high accuracy in biosensing. This can be attributed to the unique transfer technique we used that encapsulates all of the source and drain electrodes beneath a layer of parylene, with only the integrated channels and gate areas being exposed to the electrolyte environment. The on/off ratio was  $\sim 100$ , which also demonstrated the excellent performance of the semiconducting transistors. We compared the transfer curves for the before and after functionalizing of the twin-pair transistors, i.e., immobilizing the GOx with Nafion, and displayed the results in Figure 3c. The current for the sensing and reference transistors changed  $\sim 6$  and  $\sim 3\%$ , respectively, at  $V_g = 0.5$  V after functionalization. The uniformity in drain current within the twin pair is essential for the noise-cancellation strategy. Furthermore, the yields of the transistors were also high ( $\sim 95\%$ ) thanks to our use of combined fabrication techniques. Figure S5 shows the distribution of the on-current for 36 transistors in 1 batch. Even though there are variations between different twin transistors, this value within a twin pair is uniform, as indicated in Figure 3c. In general, the electrical performance of our transistors was outstanding for that of an electrolyte biosensor.

Figure 3d depicts three device structures, i.e., without parylene encapsulation (untransferred), with an external gate electrode, and with an integrated gate electrode (standard), respectively. The functioning gate electrodes are emphasized by the red dashed squares. This enables us to illustrate the benefit of encapsulating the source/drain electrode and replacing the outer gate with an integrated gate. The on-current waveforms for the three scenarios are displayed in Figure 3e, where the current fluctuation for our standard design is  $\sim 50\%$  of the untransferred case and  $\sim 32\%$  of the one with the external gate. In addition, there is inevitably tiny relative movement between the outer electrode and the transistor each time the tests are set up and are ongoing, and a fluctuation in the channel current was observed whenever the external gate electrode was used. It was therefore essential for us to eliminate this type of phenomenon and to ensure that the twin pair produced consistent results, which are independent of these types of variables because otherwise it would cause incoordination within the twin transistors. As the relative position between the gate electrode and the channel remained unchanged in our twin resistors, the electric field distribution and the transistor current remained stable, out-competing an outer gate electrode (typically Ag/AgCl) with minute movements within the electrolyte. Therefore, the integrated gate structure is essential not only for simplifying the system but also for ensuring the engineering principle. Figure 3f shows the leakage currents under the three different scenarios with respect to the different PBS concentration levels that varied between 0.1 and 10. Our standard design also had the lowest current leakage, which was  $\sim 30$  times less than those without encapsulation. And the gate leakage current increases by only 30% from 0.1× PBS to a high ion strength of 10× PBS. This demonstrated the indispensable role that the parylene encapsulating layer played. Since the stability of electrical current signals is closely related to the magnitude of drain

current and leakage current,<sup>61</sup> it is essential to create device structures that eliminate leakage current pathways. In addition, the output voltage fluctuations for both the sensing and reference transistors over time and the differential voltage waveforms (algebraic differences for the two) are shown in Figure 3g. Although there was noise and current fluctuation from both the transistors within the twin pair, the differential results in Figure 3g show a 59% reduction in standard deviations, i.e., noise value compared to the sensing readout as was indicated earlier by eq 3. The signal-to-noise ratio (SNR) is defined by the signal level divided by the noise value. As the absolute signal value is identical between sensing and differential output, the signal-to-noise ratio of the differential readout is calculated to be 2.4 times that of the sensing readout only, based on the fact that the noise level is reduced by 59%. Since the noise received by the two transistors in a twin pair is identical, ideally, this algebraic difference can generate an output voltage  $\Delta V$  solely caused in response to the target molecules in the electrolyte. In addition, there is no need for a scale factor that must be determined for each device, and so any calibration is therefore unnecessary in such a design.

For the electrical output of the integrated twin-transistor layout, Figure S6 presents the relationship between  $V_{in}$  and  $V_{out}$  of the common-source amplifier. When working in the saturation region, the transconductance  $g_m$  of the transistor is almost constant, and there is a linear relation between the input and output voltage, i.e.,

$$A_v = g_m R_d = \frac{dV_{out}}{dV_{in}} \quad (6)$$

where  $A_v$  is the amplification ratio and  $R_d$  is the resistance of the resistor. Therefore, a subtle change in the transistor current that is induced by the interaction between the receptor and the biomarker can be amplified by a factor of  $R_d$  into the output voltage, which will improve the measurement accuracy. In the case of Figure S6, the range of the input gate voltage for a linear output response was between 0.45 and 0.85 V. And the output swing ranged between 0.2 and 0.8 V. This region is depicted by the blue square. As such, the current can be tuned to 400% of the initial value and is capable of accommodating a 300% change caused by the sensing target according to eq 1.

Figure 3h displays photographs of the device being bent, twisted, and flat, respectively. To demonstrate the flexibility of the twin transistors, Figure 3i shows the transfer curves for the device before and after being repeatedly bent to a 5 mm diameter, 10 and 100 times, respectively. The current did not reveal any significant changes after being bent 10 times, but it did drop to 30% of its original value after being bent 100 times. Figure 3j shows the transfer curves before and after being repeatedly twisted 10 and 100 times using a 90° twisting angle. The results show that the current only changed by less than 6% after 100 twisting cycles. Figure 3k displays the responses for a twin transistor that was tested over 7 successive days. The transfer current shows little change, except that the effective gate voltage drifted by  $\sim 0.05$  V. These results indicate that the device is robust and is thus useful for repetitive and long-term measurements.

**Mechanism and Results of a Portable On-Skin Glucose-Sensing System.** To demonstrate a practical biosensor, we chose glucose oxidase (GOx) as our sensing agent against glucose with different concentrations in 1× PBS. The sensitivity profile of the twin transistor to glucose is shown

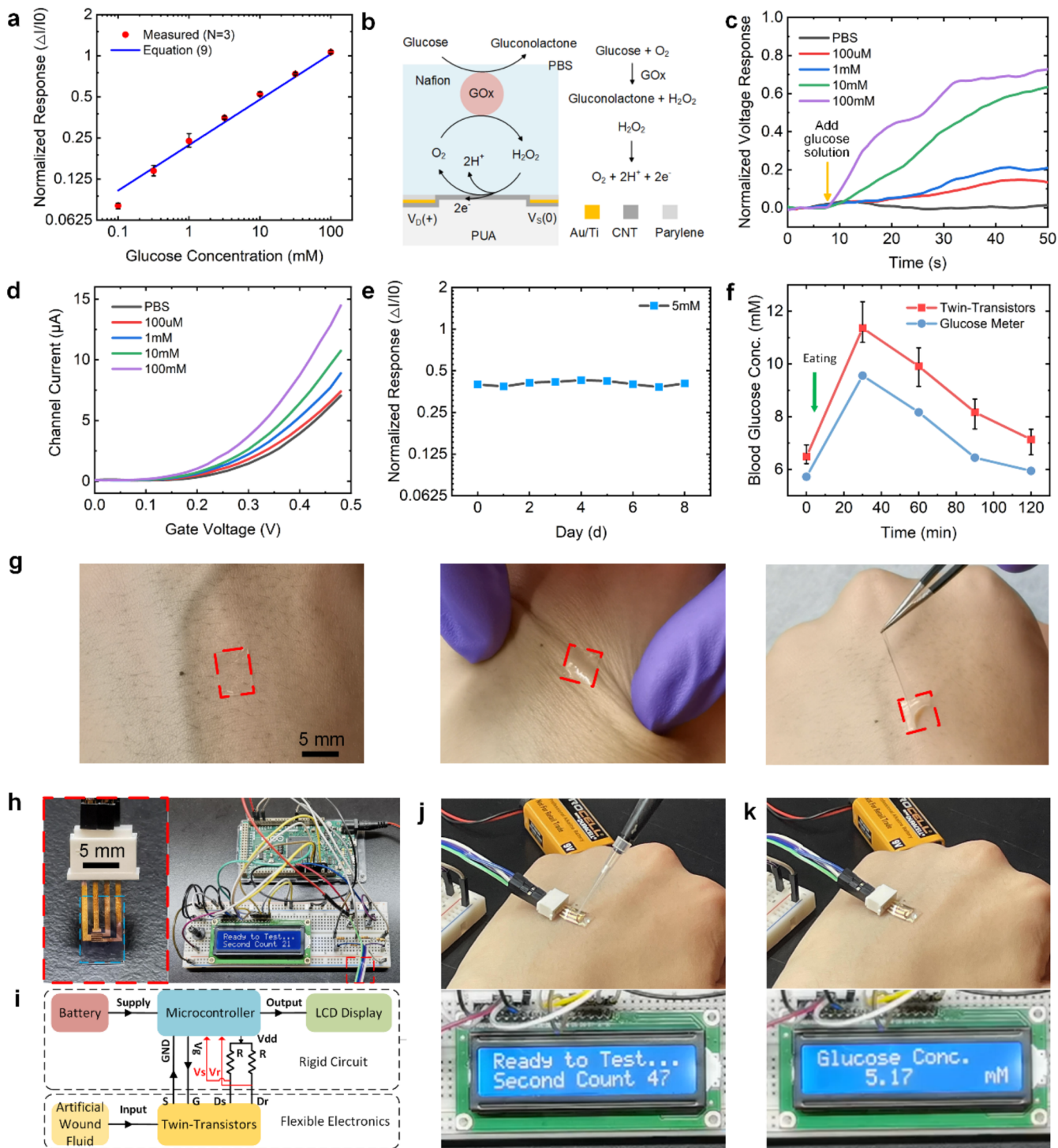


**Figure 4.** Glucose-sensing results. (a) The normalized current responses of transistors functionalized with GOx to different concentrations of glucose in 1× PBS solution. (b) Schematic of the glucose-sensing mechanism with electrons generated by electrochemical reactions. (c) The real-time voltage responses of twin transistors to glucose concentrations between 100 μM and 100 mM. (d) Responses to glucose in terms of the transfer curves of transistors functionalized with GOx. (e) Normalized glucose-sensing results over 7 days. (f) Glucose-sensing results in the serum sample tests. (g) Pictures show the stiffness variable polymer attached to the skin, being twisted and peeled off, respectively. (h) Picture of a real-time portable glucose-sensing unit containing a single-chip processing board. (i) Working mechanism of the sensing unit including the measuring, computing, and displaying system. (j) Picture of the device attached to a human hand when adding artificial wound fluid with 5 mM glucose. (k) The sensing result is displayed on a liquid crystal display (LCD).

in Figure 4a. The sensing range was large and spanned 3 orders of magnitude, which covered a human blood glucose range of roughly between 1 and 10 mM. The normalized current response was between ~0.25 and ~0.54 in this range, and the

linearity was high. The selectivity of the glucose sensor against lactate and uric acid is shown in Figure S7, where no response is observed in the range of 1 μM to 1 mM for uric acid and 100 μM to 100 mM for lactate. To further prevent the electrochemical

reaction of glucose or nonspecific adsorption of chemicals or ions on the shared Au gate electrode for reduced noise signal, several measures can be taken in future research. Surface passivation can be performed by introducing ultrathin inert coatings (e.g., poly(ethylene glycol) (PEG) or alkanethiol self-assembled monolayers) on the Au gate to further suppress nonspecific adsorption. In addition, on-chip reference integration can also be adapted to fabricate quasi-reference electrodes (e.g., Pt or carbon) to enable real-time potential compensation.

Only a single functionalized transistor is utilized in the measurement of normalized current response with a source meter. The equation for deducing normalized current response  $r_i$ , as shown in Figure 4a, from the current waveform is

$$r_i = \frac{\bar{I}(t)}{\bar{I}(t_0)} - 1 \quad (7)$$

where  $\bar{I}(t)$  and  $\bar{I}(t_0)$  refer to the stabilized current before and after adding the glucose solution, which is usually represented by the average value over 1 s with less than 10% signal variation. After we incorporate the twin-pair transistors and the differential common-source amplifier circuit, we can expect the waveform from the sensing and reference output to be  $V_s(t)$  and  $V_r(t)$ , respectively (see eqs 1 and 2). And to arrive at a value for the normalized voltage response  $r_v$ , as shown in Figure 4c, we can use the following equation

$$r_v = \frac{\bar{V}_s(t) - \bar{V}_r(t) + \bar{V}_r(t_0)}{\bar{V}_s(t_0)} - 1 \quad (8)$$

where  $\bar{V}_s(t)$ ,  $\bar{V}_s(t_0)$ ,  $\bar{V}_r(t)$ , and  $\bar{V}_r(t_0)$  correspond to the stabilized voltages of the sensing and reference transistors after and before adding a glucose solution, respectively (also represented by the average values over 1 s). And we will have a linear relationship between the current and the voltage  $V(t) = I(t) \cdot R$  at all times thanks to the common-source amplifier. As the sampling frequencies of the voltage measurements can be as high as 1 MHz, an average value of every 1000 samples can be calculated for every 1 ms. This will ensure high accuracy and low time delay for the sensing result.

For the principle behind the phenomenon of this glucose-sensing transistor, we hypothesized that the response of the channel current to the glucose concentration is due to the production of electrons during the electro-oxidation of the hydrogen peroxide that is produced in the catalyzed oxidation of the glucose by the GOx.<sup>28–30,39</sup> These electrons are conducted to SWNTs to move toward the positive drain electrodes so that the current is enhanced. The schematic explaining the sensing mechanism is shown in Figure 4b. To arrive at a plausible theoretical explanation for the electrochemical sensing mechanism, we started by analyzing the measured results. Assuming that the measured data in Figure 4a indicates a linear response, we can put them into a linear fit with any base number for a double logarithmic scale (use  $x = \log_{10} M$  and  $y = \log_2 r$ ), and we get

$$r = 0.2218M^{1/3}, \text{ or } \log_2 r = 1.1073\log_{10} M - 2.173 \quad (9)$$

In this equation,  $r$  represents the theoretical values of the normalized current responses in Figure 4a, and  $M$  is the corresponding glucose concentration with a unit of millimoles of mM. The fitting  $R^2$  is 0.9952. As the normalized current response  $r$  is unitless, the unit of  $c = 0.2218$  should be  $(\text{mM})^{-1/3}$ , i.e.,  $\text{m/mol}^{1/3}$ . This fitted line of eq 9 is shown in Figure 4a. The

slight deviation at the lowest glucose concentration, 100  $\mu\text{M}$ , could be caused by the relatively low response signal.

The response of this CNT transistor is linear on a log-log scale, which is commonly seen in liquid-gate transistors for biosensors.<sup>25,28,29</sup> The scaling of sensor response with the cubic roots of the glucose concentrations or concentration of glucose molecules in a linear dimension is intriguing. We argue that while the glucose molecule distribution in the droplet in the channel area is isotropic, only those electrons produced directly on the surface of the channel area are conducted by carbon nanotubes. In the surface area, the glucose-originated current increase in the channel width direction does not contribute to the normalized response because the base current also scales with channel width. As a result, only those electrons that are passed into the SWNTs by the electrochemical reaction along the direction of the channel length account for the normalized current. This explains the proportional relationship between the normalized current response and the cubic root of the glucose concentrations.

Since CNT is a one-dimensional (1-D) nanomaterial, its surface area is directly proportional to the density of the CNT network, and so is the drain current of the CNT-FET. In addition, glucose-induced current response is directly proportional to the surface area of the CNTs, where the electrochemical reaction takes place. Therefore, the glucose-induced current response is always proportional to the drain current without glucose, i.e., base current, eliminating the need for calibration. In other words, the results shown in Figure 4a are valid for all twin transistors regardless of the CNT network density. This feature is fundamentally different from bulk semiconducting materials, where the drain current is altered by the thickness of the material, while the target-induced response is not.

In addition, the real-time differential voltage responses to glucose are presented in Figure 4c, indicating that the responses stabilize in 40 s and that the results can be calculated in real-time. This time constant shows the typical time that is needed for an equilibrium to be reached in a chemical reaction and an ionic profile to be formed. The current responses in Figure 4a and voltage responses in Figure 4c correspond well to each other, while Figure S8 and the Supporting Information Section 2 (page S-6) explain the slight discrepancies, which could be caused by nonideal factors in the transistor.

The transfer curve response to the glucose concentrations was measured, and the results are shown in Figure 4d to reflect the traditional testing method. The current at  $V_g = V_d = 0.5$  V is generally in scale with the normalized current response shown in Figure 4a. We also characterized the stability of the sensing output over time. With the multiple tests that were conducted throughout a period of 7 days, the deviation of the output curve is still small compared to the initially calibrated one, as shown in Figure 4e, with a standard deviation of 1.58%. To further demonstrate the cyclability of this device, we calibrated the normalized response from one transistor through 7 days. The results are shown in Figure S9a, which shows good uniformity. We also conducted a real-time measurement for reversibility purposes, where 0.5  $\mu\text{L}$  of 31.6 mM glucose in PBS was added to 4.5  $\mu\text{L}$  of PBS (the glucose concentration changes from 0 to 3.16 mM). After the voltage response stabilized, 0.5 mL of PBS was added so that the voltage response decreased to near zero. The nonzero voltage is attributed to low residual glucose concentration. The performance of the new biosensor in glucose detection is compared with representative published results in

**Table S1** regarding detection limits, response linearity, sensitivity, signal acquisition method, and signal fluctuation around 3 mM (the lower limit of human blood glucose concentration range).

We also conducted glucose-sensing tests using serum samples. Human blood samples were collected at 0, 30, 60, 90, and 120 min, while food was consumed at 5 min. The blood samples were centrifuged to obtain serum, and each serum sample was tested three times to obtain an error bar, and the test results are shown in **Figure 4f** and compared with the results from a commercial glucose meter. The trend of the results measured by our transistors agrees with that of the commercial glucose meter. The deviation ranges from less than 0.8 mM at a normal blood glucose concentration at 0 min to less than 2 mM at the highest blood glucose level after eating. This deviation is attributed to calculating the serum test results by using the calibrated responses in the PBS environment. Elimination of this error is possible by calibration using serum samples with a known glucose concentration. To verify the effectiveness of the sensing in the serum environment, we recorded the real-time glucose-sensing results using human serum as a baseline while adding a glucose PBS solution to induce a change in the response voltage. The results for the real-time voltage responses are shown in **Figure S9c**, where 4  $\mu$ L of 10 mM glucose solution in PBS was added to 4  $\mu$ L of a human serum containing a normal blood glucose concentration. A stable voltage change was observed, which proved the feasibility of glucose sensing in the serum environment.

A flexible transistor was then attached to the human skin with the use of a stiffness variable polymer<sup>62</sup> to obtain conformability (see **Figures S10, S11** and Supporting Information in **Section 3**, page S-8 for more details). **Figure 4g** shows that the stiffness variable polymer displayed good conformability when the skin underneath was twisted and that it also exhibited a strong adhesion when trying to peel off the polymer. The area where the stiffness variable polymer was attached to the skin is highlighted by a red dashed square in **Figure 4g**. In addition, the **Supporting Video S1** shows the twin transistors with a variable stiffness polymer backing being attached to a human hand, where it then forms a strong adhesion due to the softening of the stiffness variable polymer triggered by the body's temperature. Cooling with water changes the polymer back into its former stiff, nonsticky state, which enables the twin transistors to be easily removed from the skin. In **Figure 4h**, the area where the stiffness variable polymer is attached to the PUA substrate is highlighted by a blue dashed square on the left of the picture.

An application of real-time stable biosensing using our flexible and conformable carbon nanotube transistors is demonstrated in **Figure 4h–k**, in which **Figure 4h** represents a picture of a portable testing system with a basic processing unit of a single-chip board. The red dashed square shows the connection to the twin transistors. The system is able to calculate glucose concentrations by reading the analog voltage outputs from the transistors and showing the results on a liquid crystal display (LCD). **Figure 4i** is a diagram of the measuring system, and the Supporting Information **Section 4** (page S-10) explains the working principles of this system. The differential outputs from the common-source amplifier are read by a single-chip board, which reflects the changes in the concentration levels of glucose above the channel area.

Even though this device possesses flexibility and conformability, the serum is the only human-originated biofluid that was tested and required *in vitro* experiments. This means that the

wearable potential is not fully realized for noninvasive measurements. To depict a practical on-skin scenario, we chose artificial wound fluid as the carrying medium for the glucose, and the calibrated response is shown in **Figure S12**. The twin transistors displayed good sensing linearity in the artificial wound fluid's environment, while the sensitivity was higher than that in the PBS. The enhanced sensitivity was due to the lower ion concentration in the artificial wound fluid, which lowered the baseline current. **Figure 4j,4k** shows the sequential process for the artificial wound fluid being added to the sensing device's channel area through a pipet, and the sensor's result of 5.17 mM is displayed on the LCD after 60 s. The real-time response feature with high stability can be further observed in **Supporting Video S2**. The whole system was constructed with simple electrical components in which the only additional items were the resistors and battery, and no large-scale equipment such as a source meter, computer, or even an oscilloscope was used. The direct current (DC) voltages required for the measuring circuit were provided by the single-chip board. With all of the measuring, computing, and displaying modules powered by a battery, this compact system is portable and has the potential to be miniaturized at low cost.

## CONCLUSIONS

In summary, flexible and conformable carbon nanotube twin transistors have been successfully fabricated via a process combining microfabrication, solution-based processing, and transfer. The process is fairly robust, with a 95% device yield. We achieved the high-resolution patterning of SWNTs by using a PDMS contact mask and adhered the entire parylene substrate to the PUA matrix by applying TMSPMA. The twin transistor design improves the tolerance of the sensing responses to the distribution nonuniformity of the SWNTs networks in the channel and thus improves the process yield. The integrated sensor structure features encapsulating layers to minimize electrolytic current leakage, an integrated gate electrode for a stable result, a twin-transistor pair for accurate output, and a common-source amplifier for a real-time response. For glucose sensing, a Nafion polymer coating immobilizes glucose oxidase within a designated area of the integrated sensor channel. The normalized responses are linear to the cubic root of the glucose concentration between 0.1 and 100 mM. Detection of glucose concentrations that are even lower is limited by the low response of the signals, while efforts to enhance the responses by further increasing the GOx density were hampered due to its limited solubility in water during immobilization. The cubic root proportionality supports the one-directional conduction mechanism of the SWNTs in the sensor channel length direction. The robust sensor response, simplified circuit, and no requirement for any device-specific calibration allowed for a portable glucose measuring system to be demonstrated. Larger data sets and controls are needed in future work to assess interference existing in complex biological fluids for selectivity concerns.

## METHODS

**Materials.** 99.9% of the SWNT dispersion was purchased from Nanointegris. The CN990 and SRS40 were purchased from Sartomer. All other chemicals were purchased from Sigma-Aldrich.

**Preparation of the SWNT Dispersion and Polyurethane Acrylate (PUA) Precursor.** The 99.9% semiconducting carbon nanotube solution was used as received. Oligomer CN990, sartomer SRS40, and photoinitiator 2,2-dimethoxy-2-phenylacetophenone

(DMPA) were mixed with a weight ratio of 100:20:1. The mixture was ultrasonicated for 24 h to obtain a uniform precursor.

**Fabrication of the Flexible and Conformable Carbon Nanotube Transistors.** 500 nm thick parylene C film and 100 nm Au and 20 nm Ti layers were deposited onto a clean glass substrate sequentially by chemical vapor deposition and vacuum evaporation, respectively. A first photolithography was performed to wet etch the metal layers to define the interdigitated electrode patterns for the transistors. A second photolithography was performed to define the channel areas in which the parylene layer was etched using oxygen plasma. A laser-cut PDMS contact mask with openings in the channel area was aligned to the substrate. The sample was then treated with oxygen plasma of 18W for 3 min to make the channel areas hydrophilic, thus being able to achieve uniform SWNT distribution in a later step. 25  $\mu\text{L}$  of prepared semiconducting SWNT dispersion was applied to each device pair, and 5  $\mu\text{L}$  was drop-casted each time onto the shared channel area 5 times with a 5 min interval at 100 °C. Five minutes after the last round of drop-casting, the mask was peeled off from the sample after it cooled, and the sample was rinsed carefully for 30 s and dried at 100 °C for 1 min. 3-(Trimethoxysilyl) propyl methacrylate in toluene with a volume ratio of 1:3 was applied to the margin area of the sample slide using a Q-tip. An inkjet mold was prepared with a 170  $\mu\text{m}$  spacer and preheated to 90 °C together with the PUA precursor. PUA precursor was injected into the mold, and the sample was kept at 90 °C for 5 min to fully embed the SWNT network into the polymer matrix. After this, the sample was cooled and UV-cured for 150 s, and then it was immersed in deionized (DI) water overnight. One side of the glass of the inkjet mold was carefully peeled off with the parylene side upward and blown dry with air. Another PDMS contact mask with openings for the electrode contacts and integrated gate exposure area was aligned with the sample. Oxygen plasma treatment with 300 W and 300 mTorr for 3 min was applied to etch away the defined parylene area to expose the metal electrodes to complete the fabrication and for measurement purposes. The flexible and conformable carbon nanotube transistor was ready after the mask was removed, and it was peeled off from the glass substrate.

**Functionalization Process Using the Polymer to Cover the Sensing Agent.** The glucose oxidase (GOx) was physically immobilized using a thin film of Nafion polymer. 1 mg of GOx was dissolved in 200  $\mu\text{L}$  of phosphate-buffered saline (PBS) and kept at 4 °C. A 0.5% Nafion solution was prepared by diluting 5% Nafion solution with DI water. 5  $\mu\text{L}$  of GOx solution was applied to each channel area and dried at 4 °C for 12 h. Then, the sample was coated with 5  $\mu\text{L}$  of Nafion solution applied to each channel area. And the sample was dried at 4 °C for 12 h. The functionalization process was finished, carefully rinsed two times, and dried.

**Preparation for Testing the Electrolytes Using Different Glucose Concentrations in PBS.** Glucose solutions of different concentrations in 1× PBS were, respectively, prepared to test their responses to the GOx glucose oxidase in the transistor that was acting as the glucose sensor. Four microliters of glucose solution was applied to the channel area for each test.

**Measurement Setup for Measuring Performance Characteristics of a Unit Device.** A keysight B2902B source meter was used for the two-channel driving and measurement. A drain voltage between 0 and 0.8 V and a gate voltage between 0 and 0.5 V were applied to derive the output and transfer characteristics of a unit transistor. Four  $\mu\text{L}$  of 1× PBS was applied to the channel area and the integrated gate for each test.

**Measurement Setup for Obtaining the Direct Voltage Readouts from the Twin Transistors.** The gate and source electrodes of the twin transistors were connected to the source meter, respectively. The normal position for the drain electrode was connected to a  $V_{DD}$ . Probes from the HS4 oscilloscope were connected to the drain electrodes of the twin transistor, gate electrode, and  $V_{DD}$ , respectively. A common-source amplifier layout was adopted with differential readout from the drain electrodes. The resistors were set at 200 k $\Omega$ . The current through the transistors was amplified as was the voltage across the resistors. In addition, the different functionalized statuses of the twin pair acted as the differential input. The gate voltage

and  $V_{DD}$  were set at 0.5 and 1 V, respectively, while the source electrode was connected to GND. Four microliters of glucose with different concentrations in 1× PBS solutions were applied to the channel area and the integrated gate electrode for each test.

**Human Blood Sample Collection and Serum Testing Using the Twin Transistors.** A lancing device from a commercial glucose meter was used to puncture a human finger. 100  $\mu\text{L}$  of blood was collected and centrifuged at 1250 rcf for 15 min. About 20  $\mu\text{L}$  of serum was then removed from the blood sample and tested in the same way as the glucose dissolved in PBS.

**Artificial Wound Fluid Glucose Measurement Using a Portable System.** The flexible twin transistors were attached to a human hand with the stiff variable polymer on the back side. 4  $\mu\text{L}$  of artificial wound fluid was added to the channel area, and then the start button was pressed. After 60 s of waiting time, glucose concentration was calculated, and the result was shown on an LCD display.

**Preparation of PBS.** 1× PBS and 0.1× PBS are diluted from 10× PBS 10 and 100 times, respectively.

**Preparation of Artificial Wound Fluid.** 0.627 g of sodium hydrogen carbonate, 1.1688 g of sodium chloride, 0.06 g of potassium chloride, 0.096 g of calcium chloride, and 6.6 g of bovine serum albumin (BSA) are dissolved in deionized water to form a 200 mL artificial wound fluid. And it is kept at 4 °C.

## ASSOCIATED CONTENT

### Supporting Information

The Supporting Information is available free of charge at <https://pubs.acs.org/doi/10.1021/acsanm.5c01165>.

Working principle of differential common-source amplifier circuit; circuit diagram of differential common-source amplifier circuit (Figure S1); detailed schematics of the fabrication process (Figure S2); geometry, optical picture, and SEM image of the device (Figure S3); additional electrical characterization of the transistor (Figure S4); on-current distribution chart for 36 transistors in one batch (Figure S5); relationship between  $V_{in}$  and  $V_{out}$  as a basic property of a common-source amplifier (Figure S6); selectivity of the glucose sensor against lactate and uric acid (Figure S7); explanation for discrepancy between normalized current and differential voltage response; nonideal factor of transistors (Figure S8); additional glucose-sensing characterizations (Figure S9); features of the modulus variable polymer; characterizations of the stiffness variable polymer, Young's modulus vs temperature of a stiffness variable material<sup>62</sup> (Figure S10); picture showing the tight bonding between the polymer with human skin (Figure S11); working principle of the portable glucose measuring circuit; calibrated sensing response to glucose in artificial wound fluid environment (Figure S12); comparison between this work and representative publications for glucose sensing in terms of key sensing parameters; and S/D electrodes in the table mean source/drain electrodes (Table S1) (PDF)

Twin transistors with a variable stiffness polymer backing being attached to a human hand (MP4)

Real-time response feature of the twin transistors with high stability (MP4)

## AUTHOR INFORMATION

### Corresponding Author

Qibing Pei – Department of Materials Sciences and Engineering, Henry Samueli School of Engineering and Applied Science, University of California, Los Angeles, California 90095, United States; [orcid.org/0000-0003-1669-1734](https://orcid.org/0000-0003-1669-1734); Email: [qpei@seas.ucla.edu](mailto:qpei@seas.ucla.edu)

**Authors**

**Hanxiang Wu** — Department of Materials Sciences and Engineering, Henry Samueli School of Engineering and Applied Science, University of California, Los Angeles, California 90095, United States;  [orcid.org/0000-0002-8556-8468](https://orcid.org/0000-0002-8556-8468)

**Yu Song** — Andrew and Peggy Cherng Department of Medical Engineering, California Institute of Technology, Pasadena, California 91125, United States

**Hexing Yin** — Department of Materials Sciences and Engineering, Henry Samueli School of Engineering and Applied Science, University of California, Los Angeles, California 90095, United States

**Yuan Zhu** — Department of Materials Sciences and Engineering, Henry Samueli School of Engineering and Applied Science, University of California, Los Angeles, California 90095, United States

**Ao Zhang** — Department of Materials Sciences and Engineering, Henry Samueli School of Engineering and Applied Science, University of California, Los Angeles, California 90095, United States

**Zhixin Xie** — Department of Materials Sciences and Engineering, Henry Samueli School of Engineering and Applied Science, University of California, Los Angeles, California 90095, United States

**Canran Wang** — Andrew and Peggy Cherng Department of Medical Engineering, California Institute of Technology, Pasadena, California 91125, United States

**Meng Gao** — Department of Materials Sciences and Engineering, Henry Samueli School of Engineering and Applied Science, University of California, Los Angeles, California 90095, United States;  [orcid.org/0000-0002-3018-6657](https://orcid.org/0000-0002-3018-6657)

**Wei Gao** — Andrew and Peggy Cherng Department of Medical Engineering, California Institute of Technology, Pasadena, California 91125, United States;  [orcid.org/0000-0002-8503-4562](https://orcid.org/0000-0002-8503-4562)

Complete contact information is available at:

<https://pubs.acs.org/10.1021/acsanm.5c01165>

**Author Contributions**

Conceptualization: H.W. and Q.P.; methodology: H.W.; investigation: H.W., Y.S. H.Y., Y.Z., A.Z., Z.X., C.W., and M.G.; writing—original draft: H.W.; writing—review and editing: Q.P., W.G., Y.S., and Y.Z.; funding acquisition, Q.P.; and resources: Q.P. and W.G.; and supervision: Q.P.

**Notes**

The authors declare no competing financial interest.

**ACKNOWLEDGMENTS**

The authors acknowledge financial support from the National Robotic Initiative Program of the National Science Foundation (Award no. 1638163) and NIH National Eye Institute award # 1R01EY030246-01A1. The authors acknowledge the use of instruments at the cleanroom of California NanoSystems Institute (CNSI) and the Electron Imaging Center for NanoMachines (EICN) at UCLA.

**REFERENCES**

- (1) Balasubramanian, K.; Burghard, M. *Carbon Nanotubes: Methods and Protocols*; Humana Press: New York, 2010; pp 1–253.
- (2) Sun, D. M.; Liu, C.; Ren, W. C.; Cheng, H. M. A review of carbon nanotube-and graphene-based flexible thin-film transistors. *Small* **2013**, *9* (8), 1188–1205.
- (3) Yang, F.; Zhang, G. J. Silicon nanowire-transistor biosensor for study of molecule-molecule interactions. *Rev. Anal. Chem.* **2014**, *33* (2), 95–110.
- (4) Vu, C. A.; Chen, W. Y. Field-effect transistor biosensors for biomedical applications: recent advances and future prospects. *Sensors* **2019**, *19* (19), 4214.
- (5) Zhu, Z. An overview of carbon nanotubes and graphene for biosensing applications. *Nano-Micro Lett.* **2017**, *9* (3), No. 25.
- (6) Tey, J. N.; Wijaya, I. P. M.; Wei, J.; Rodriguez, I.; Mhaisalkar, S. G. Nanotubes-/nanowires-based, microfluidic-integrated transistors for detecting biomolecules. *Microfluid. Nanofluid.* **2010**, *9* (6), 1185–1214.
- (7) Allen, B. L.; Kichambare, P. D.; Star, A. Carbon nanotube field-effect-transistor-based biosensors. *Adv. Mater.* **2007**, *19* (11), 1439–1451.
- (8) Pourasl, A. H.; Ahmadi, M. T.; Rahmani, M.; Chin, H. C.; Lim, C. S.; Ismail, R.; Tan, M. L. P. Analytical modeling of glucose biosensors based on carbon nanotubes. *Nanoscale Res. Lett.* **2014**, *9* (1), No. 33.
- (9) Wooten, M.; Karra, S.; Zhang, M.; Gorski, W. On the direct electron transfer, sensing, and enzyme activity in the glucose oxidase/carbon nanotubes system. *Anal. Chem.* **2014**, *86* (1), 752–757.
- (10) Rahmani, M.; Ghafoori Fard, H.; Ahmadi, M. T.; Rahmani, K. Analytical prediction of carbon nanoscroll-based electrochemical glucose biosensor performance. *Int. J. Environ. Anal. Chem.* **2017**, *97* (11), 1024–1036.
- (11) Gupta, S.; Murthy, C. N.; Prabha, C. R. Recent advances in carbon nanotube based electrochemical biosensors. *Int. J. Biol. Macromol.* **2018**, *108*, 687–703.
- (12) Dai, B.; Zhou, R.; Ping, J.; Ying, Y.; Xie, L. Recent advances in carbon nanotube-based biosensors for biomolecular detection. *TrAC, Trends Anal. Chem.* **2022**, *154*, No. 116658.
- (13) Ranjbari, S.; Bolourinezhad, M.; Kesharwani, P.; Rezayi, M.; Sahebkar, A. Applications of carbon nanotube biosensors: Sensing the future. *J. Drug Delivery Sci. Technol.* **2024**, *97*, No. 105747.
- (14) Zamzami, M. A.; Rabbani, G.; Ahmad, A.; Basalah, A. A.; Al-Sabban, W. H.; Ahn, S. N.; Choudhry, H. Carbon nanotube field-effect transistor (CNT-FET)-based biosensor for rapid detection of SARS-CoV-2 (COVID-19) surface spike protein S1. *Bioelectrochemistry* **2022**, *143*, No. 107982.
- (15) Berto, M.; Di Giosia, M.; Giordani, M.; Sensi, M.; Valle, F.; Alessandrini, A.; Bortolotti, C. A.; et al. Green Fabrication of (6, 5) Carbon Nanotube/Protein Transistor Endowed with Specific Recognition. *Adv. Electron. Mater.* **2021**, *7* (5), No. 2001114.
- (16) Liang, Y.; Xiao, M.; Wu, D.; Lin, Y.; Liu, L.; He, J.; Zhang, Z.; et al. Wafer-scale uniform carbon nanotube transistors for ultrasensitive and label-free detection of disease biomarkers. *ACS Nano* **2020**, *14* (7), 8866–8874.
- (17) Hatada, M.; Tran, T. T.; Tsugawa, W.; Sode, K.; Mulchandani, A. Affinity sensor for haemoglobin A1c based on single-walled carbon nanotube field-effect transistor and fructosyl amino acid binding protein. *Biosens. Bioelectron.* **2019**, *129*, 254–259.
- (18) Fatin, M. F.; Ruslinda, A. R.; Gopinath, S. C.; Arshad, M. M. High-performance interactive analysis of split aptamer and HIV-1 Tat on multiwall carbon nanotube-modified field-effect transistor. *Int. J. Biol. Macromol.* **2019**, *125*, 414–422.
- (19) Chen, H.; Xiao, M.; He, J.; Zhang, Y.; Liang, Y.; Liu, H.; Zhang, Z. Aptamer-functionalized carbon nanotube field-effect transistor biosensors for Alzheimer's disease serum biomarker detection. *ACS Sens.* **2022**, *7* (7), 2075–2083.
- (20) Lee, M.; Kim, D. Exotic carbon nanotube based field effect transistor for the selective detection of sucrose. *Mater. Lett.* **2020**, *268*, No. 127571.
- (21) Besteman, K.; Lee, J. O.; Wiertz, F. G.; Heering, H. A.; Dekker, C. Enzyme-coated carbon nanotubes as single-molecule biosensors. *Nano Lett.* **2003**, *3* (6), 727–730.
- (22) He, J.; Cao, X.; Liu, H.; Liang, Y.; Chen, H.; Xiao, M.; Zhang, Z. Power and Sensitivity Management of Carbon Nanotube Transistor Glucose Biosensors. *ACS Appl. Mater. Interfaces* **2024**, *16* (1), 1351–1360.

- (23) Joshi, S.; Bhatt, V. D.; Wu, H.; Becherer, M.; Lugli, P. Flexible lactate and glucose sensors using electrolyte-gated carbon nanotube field effect transistor for non-invasive real-time monitoring. *IEEE Sens. J.* **2017**, *17* (14), 4315–4321.
- (24) Altuntas, H.; Snashall, K.; Oke-Altuntas, F.; Jayawardane, I.; Tas, M. O.; Silva, S. R. P. Effect of pyrene-1 boronic acid functionalization on the electrical characteristics of carbon nanotube field-effect transistor. *Electron. Mater. Lett.* **2023**, *19* (5), 405–414.
- (25) Khan, M.; Nagal, V.; Masrat, S.; Tuba, T.; Alam, S.; Bhat, K. S.; Wahid, I.; Ahmad, R. Vertically oriented zinc oxide nanorod-based electrolyte-gated field-effect transistor for high-performance glucose sensing. *Anal. Chem.* **2022**, *94* (25), 8867–8873.
- (26) Nakatsuka, N.; Yang, K. A.; Abendroth, J. M.; Cheung, K. M.; Xu, X.; Yang, H.; Andrews, A. M.; et al. Aptamer–field-effect transistors overcome Debye length limitations for small-molecule sensing. *Science* **2018**, *362* (6412), 319–324.
- (27) Wang, B.; Luo, Y.; Gao, L.; Liu, B.; Duan, G. High-performance field-effect transistor glucose biosensors based on bimetallic Ni/Cu metal-organic frameworks. *Biosens. Bioelectron.* **2021**, *171*, No. 112736.
- (28) Bhat, K. S.; Ahmad, R.; Yoo, J. Y.; Hahn, Y. B. Nozzle-jet printed flexible field-effect transistor biosensor for high performance glucose detection. *J. Colloid Interface Sci.* **2017**, *506*, 188–196.
- (29) Liu, Q.; Liu, Y.; Wu, F.; Cao, X.; Li, Z.; Alharbi, M.; Zhou, C.; et al. Highly sensitive and wearable In<sub>2</sub>O<sub>3</sub> nanoribbon transistor biosensors with integrated on-chip gate for glucose monitoring in body fluids. *ACS Nano* **2018**, *12* (2), 1170–1178.
- (30) You, X.; Pak, J. J. Graphene-based field effect transistor enzymatic glucose biosensor using silk protein for enzyme immobilization and device substrate. *Sens. Actuators, B* **2014**, *202*, 1357–1365.
- (31) Pacios, M.; Martin-Fernandez, I.; Borrisé, X.; del Valle, M.; Bartrolí, J.; Lora-Tamayo, E.; Esplandiu, M. J.; et al. Real time protein recognition in a liquid-gated carbon nanotube field-effect transistor modified with aptamers. *Nanoscale* **2012**, *4* (19), 5917–5923.
- (32) Li, C.; Curreli, M.; Lin, H.; Lei, B.; Ishikawa, F. N.; Datar, R.; Zhou, C.; et al. Complementary detection of prostate-specific antigen using In<sub>2</sub>O<sub>3</sub> nanowires and carbon nanotubes. *J. Am. Chem. Soc.* **2005**, *127* (36), 12484–12485.
- (33) So, H. M.; Won, K.; Kim, Y. H.; Kim, B. K.; Ryu, B. H.; Na, P. S.; Kim, H.; Lee, J. O. Single-walled carbon nanotube biosensors using aptamers as molecular recognition elements. *J. Am. Chem. Soc.* **2005**, *127* (34), 11906–11907.
- (34) Park, J. W.; Lee, C.; Jang, J. High-performance field-effect transistor-type glucose biosensor based on nanohybrids of carboxylated polypyrrole nanotube wrapped graphene sheet transducer. *Sens. Actuators, B* **2015**, *208*, 532–537.
- (35) Tung, N. T.; Tue, P. T.; Thi Ngoc Lien, T.; Ohno, Y.; Maehashi, K.; Matsumoto, K.; Takamura, Y.; et al. Peptide aptamer-modified single-walled carbon nanotube-based transistors for high-performance biosensors. *Sci. Rep.* **2017**, *7* (1), No. 17881.
- (36) Nguyen, H. P. T.; Murugathas, T.; Plank, N. O. Comparison of Duplex and Quadruplex Folding Structure Adenosine Aptamers for Carbon Nanotube Field Effect Transistor Aptasensors. *Nanomaterials* **2021**, *11* (9), 2280.
- (37) Sharf, T.; Kevek, J. W.; DeBorde, T.; Wardini, J. L.; Minot, E. D. Origins of charge noise in carbon nanotube field-effect transistor biosensors. *Nano Lett.* **2012**, *12* (12), 6380–6384.
- (38) Zheng, H. Y.; Alsager, O. A.; Zhu, B.; Trivas-Sejdic, J.; Hodgkiss, J. M.; Plank, N. O. Electrostatic gating in carbon nanotube aptasensors. *Nanoscale* **2016**, *8* (28), 13659–13668.
- (39) Lee, D.; Cui, T. Low-cost, transparent, and flexible single-walled carbon nanotube nanocomposite based ion-sensitive field-effect transistors for pH/glucose sensing. *Biosens. Bioelectron.* **2010**, *25* (10), 2259–2264.
- (40) Zheng, H. Y.; Alsager, O. A.; Wood, C. S.; Hodgkiss, J. M.; Plank, N. O. Carbon nanotube field effect transistor aptasensors for estrogen detection in liquids. *J. Vac. Sci. Technol., B:Nanotechnol. Microelectron.: Mater., Process., Meas., Phenom.* **2015**, *33* (6), No. 06F904.
- (41) Liao, J.; Lin, S.; Yang, Y.; Liu, K.; Du, W. Highly selective and sensitive glucose sensors based on organic electrochemical transistors using TiO<sub>2</sub> nanotube arrays-based gate electrodes. *Sens. Actuators, B* **2015**, *208*, 457–463.
- (42) Abe, M.; Murata, K.; Ataka, T.; Matsumoto, K. Calibration method for a carbon nanotube field-effect transistor biosensor. *Nanotechnology* **2008**, *19* (4), No. 045505.
- (43) Ma, S.; Zhang, Y.; Ren, Q.; Wang, X.; Zhu, J.; Yin, F.; Li, Z.; Zhang, M. Tetrahedral DNA nanostructure based biosensor for high-performance detection of circulating tumor DNA using all-carbon nanotube transistor. *Biosens. Bioelectron.* **2022**, *197*, No. 113785.
- (44) Wang, C.; Cui, X.; Li, Y.; Li, H.; Huang, L.; Bi, J.; Miao, F.; et al. A label-free and portable graphene FET aptasensor for children blood lead detection. *Sci. Rep.* **2016**, *6* (1), No. 21711.
- (45) Nawaz, A.; Liu, Q.; Leong, W. L.; Fairfull-Smith, K. E.; Sonar, P. Organic Electrochemical Transistors for In Vivo Bioelectronics. *Adv. Mater.* **2021**, *33* (49), No. 2101874.
- (46) Albarghouthi, F. M.; Semeniak, D.; Khanani, I.; Doherty, J. L.; Smith, B. N.; Salfity, M.; Franklin, A. D.; et al. Addressing Signal Drift and Screening for Detection of Biomarkers with Carbon Nanotube Transistors. *ACS Nano* **2024**, *18* (7), 5698–5711.
- (47) Luo, Y.; Abidian, M. R.; Ahn, J. H.; Akinwande, D.; Andrews, A. M.; Antonietti, M.; Chen, X.; et al. Technology roadmap for flexible sensors. *ACS Nano* **2023**, *17* (6), 5211–5295.
- (48) Sakata, T. Signal transduction interfaces for field-effect transistor-based biosensors. *Commun. Chem.* **2024**, *7* (1), No. 35.
- (49) Hao, Z.; Luo, Y.; Huang, C.; Wang, Z.; Song, G.; Pan, Y.; Zhao, X.; Liu, S. An Intelligent Graphene-Based Biosensing Device for Cytokine Storm Syndrome Biomarkers Detection in Human Biofluids. *Small* **2021**, *17* (29), No. 2101508.
- (50) Wang, Y.; Wang, T.; Xiang, L.; Huang, R.; Long, G.; Wang, W.; Hu, Y. Sub-180-nanometer-thick ultraconformable high-performance carbon nanotube-based dual-gate transistors and differential amplifiers. *Sci. Adv.* **2024**, *10* (36), No. eadq6022.
- (51) Hou, B.; Radadia, A. D. Differential stability of biosensing proteins on transferred mono/bilayer graphene. *ACS Biomater. Sci. Eng.* **2018**, *4* (2), 675–681.
- (52) Ushiba, S.; Nakano, T.; Shinagawa, A.; Miyakawa, N.; Kato, T.; Yofu, K.; Matsumoto, K.; et al. Biosensing with Surface-Charge-Modulated Graphene Field-Effect Transistors beyond Nonlinear Electrolytic Screening. *ACS Omega* **2023**, *8* (51), 49270–49277.
- (53) Tsai, K. Y.; Peng, H. F.; Huang, J. J. Nafion modified electrochemical sensor integrated with a feedback-loop indium-gallium-zinc oxide thin-film transistor for enhancing dopamine detection limit. *Sens. Actuators, A* **2023**, *354*, No. 114287.
- (54) Lee, H. H.; Bae, M.; Jo, S. H.; Shin, J. K.; Son, D. H.; Won, C. H.; Lee, J. H. Differential-mode HEMT-based biosensor for real-time and label-free detection of C-reactive protein. *Sens. Actuators, B* **2016**, *234*, 316–323.
- (55) Satake, H.; Sakata, T. Estimation of extracellular matrix production using a cultured-chondrocyte-based gate ion-sensitive field-effect transistor. *Anal. Chem.* **2019**, *91* (24), 16017–16022.
- (56) Tyrrell, J. E.; Petkos, K.; Drakakis, E. M.; Boutelle, M. G.; Campbell, A. J. Organic Electrochemical Transistor Common-Source Amplifier for Electrophysiological Measurements. *Adv. Funct. Mater.* **2021**, *31* (33), No. 2103385.
- (57) Zhu, C.; Chortos, A.; Wang, Y.; Pfattner, R.; Lei, T.; Hinckley, A. C.; Murmann, B.; et al. Stretchable temperature-sensing circuits with strain suppression based on carbon nanotube transistors. *Nat. Electron.* **2018**, *1* (3), 183–190.
- (58) Zhang, H.; Yuan, Y.; Hu, J.; Xiang, L. Advances of Carbon Nanotube Based Flexible Amplifiers for Skin-Mounted Physiological Signal Monitoring. *Adv. Electron. Mater.* **2025**, No. 2400991.
- (59) Sugiyama, M.; Uemura, T.; Kondo, M.; Akiyama, M.; Namba, N.; Yoshimoto, S.; Sekitani, T.; et al. An ultraflexible organic differential amplifier for recording electrocardiograms. *Nat. Electron.* **2019**, *2* (8), 351–360.
- (60) Kondo, M.; Uemura, T.; Akiyama, M.; Namba, N.; Sugiyama, M.; Noda, Y.; Sekitani, T. In *Design of Ultraflexible Organic Differential Amplifier Circuits for Wearable Sensor Technologies*, 2018 IEEE

International Conference on Microelectronic Test Structures (ICMTS); IEEE, 2018; pp 79–84.

(61) Sakata, T.; Nishitani, S.; Saito, A.; Fukasawa, Y. Solution-gated ultrathin channel indium tin oxide-based field-effect transistor fabricated by a one-step procedure that enables high-performance ion sensing and biosensing. *ACS Appl. Mater. Interfaces* **2021**, *13* (32), 38569–38578.

(62) Gao, M.; Wu, H.; Plamthottam, R.; Xie, Z.; Liu, Y.; Hu, J.; Pei, Q.; et al. Skin temperature-triggered, debonding-on-demand sticker for a self-powered mechanosensitive communication system. *Matter* **2021**, *4* (6), 1962–1974.

CAS INSIGHTS™  
EXPLORE THE INNOVATIONS SHAPING TOMORROW

Discover the latest scientific research and trends with CAS Insights. Subscribe for email updates on new articles, reports, and webinars at the intersection of science and innovation.

Subscribe today

**CAS**  
A division of the American Chemical Society